Ocean Engineering
May 2024, Volume 299 Pages 117363 (11p.)
https://doi.org/10.1016/j.oceaneng.2024.117363
https://archimer.ifremer.fr/doc/00881/99327/

Multi-objective optimization of cycloidal blade-controlled propeller: An experimental approach

Fasse Guillaume [1, *], Sacher Matthieu [2], Hauville Frederic [1], Astolfi Jacques-Andre [1], Germain Gregory [3]

[1] Naval Academy Research Institute (IRENav), BCRM Brest, CC600, 29240 Brest Cedex9, France
[2] ENSTA Bretagne, CNRS UMR 6027, IRDL, 2 rue Francois Verny, 29806 Brest Cedex9, France
[3] IFREMER, LHyMar Laboratory, 62200 Boulogne-sur-Mer, France

* Corresponding author : Guillaume Fasse, email address : guillaume.fasse@ensta-bretagne.fr

Abstract :

In recent years, innovative naval propulsion systems have been investigated thanks to the growing development of unmanned underwater vehicles. Cycloidal propellers are promising alternative concepts to the usual screw propellers. As bio-inspired technology, these systems use mechanical energy from unsteady hydrodynamic forces generated by blades oscillation like natural marine animal swimmers. As an academic platform, the French Naval Academy Research Institute developed a large-scale experimental cycloidal propeller with the aim of running various pitch motions to evaluate performances of cross-flow propellers. Blades' pitching is here performed by servo-motors in order to control each blade independently. While common cycloidal propellers use mechanical blade actuators which restrain the blade motion possibilities, this blade-controlled platform allows new investigations of interesting research area in marine propulsion. The platform is widely instrumented with load and torque sensors to measure instantaneous hydrodynamic forces during the rotation of the blades. Experiments, performed in a current flume tank, first reveal that for classical sinusoidal pitch laws, performances are depending on the operating point: the higher the advance parameter, the lower the sinusoidal amplitude must be for a better efficiency. These results confirm the requirement of an adaptable pitch control for cycloidal propeller to improve their performances regarding the operation mode. To go further, an experimental optimization, based on surrogate models (Efficient Global Optimization), is undertaken to surpass the performance of the propeller with parameterized pitch laws. This method authorizes a wide range of possible motion taking account of the platform speed limits. Multi-objective optimization is performed for total thrust and efficiency maximizing for two operating points. Results on the Pareto fronts show that a trade-off is necessary between thrust and efficiency concerning. However, optimized pitching laws reveal high hydrodynamic performances, with gains respectively from 10% to 20% on the hydrodynamic efficiency and the thrust in comparison with classic sinusoidal laws. This confirms the benefit of full electrical blade-controlled propeller and promises interesting further investigations on the experimental optimization.

Highlights

► Improving performances of cycloidal propeller. ► Electrical Blade-controlled platform. ► Multi-objective experimental optimization with gaussian process. ► Experimental measurement of local hydrodynamic forces on cross-flow propeller blades.

Keywords : Cycloidal propulsion, Blade-control, Experimental optimization, Parametric pitch laws, Multi-objective optimization, Pareto front compromise

1. Introduction

Innovative naval propellers are nowadays widely explored thanks to the growing development of unmanned underwater vehicles and new naval needs and constraints like noise and consumption reduction. Reduction of green house gas require significantly improving the propulsive efficiency (Theotokatos and Tzelepis, 2015) and specific development for optimizing propellers like done in Doijode et al. (2022) for conventional propeller blades. Another way is to develop other propulsive architectures and cycloidal propellers are promising alternative concepts to the usual screw propellers.

Cycloidal propellers are characterized by the rotation of several blades around an axis perpendicular to the ship advance direction (this type of propulsion is also named cross-flow propeller). This first rotation is called main rotation, given by the rotational speed and related to the azimuth angle. Each blade is also rotating around their own axis during the main rotation of the whole system (like helicopter's blades). This secondary rotation is called pitch rotation, related to the blade pitch angle. The combination of these two rotations reproduces the motion of natural marine swimmers, especially studied by Triantafyllou et al. (2004). This particular motion creates strong unsteady hydrodynamic forces

which produce lift and drag during the main rotation. For propulsive purpose, the part of hydrodynamic force in the direction of the ship advance produces the thrust force whereas the part in the perpendicular direction is called side force. These propellers can easily orientate the thrust over 360° by shifting the blade pitch law over the main rotation angle.

For this type of propulsion, two kinematic modes are commonly defined according to the advance parameter λ which is the ratio of the ship advance speed V_a and the blade peripheral speed V_r:

$$\lambda = \frac{V_a}{V_r} \tag{1}$$

Epicycloidal mode is defined for λ <1 (Figure 1). For this mode, peripheral speed is higher than advance speed. This mode produces a high thrust and strong maneuverability for low advance speed (limited by the maximal main rotation speed). On the other hand, trochoidal mode defined for λ >1 (Figure 2), is used to reach higher advance speed but with a lack of efficiency during starting phases (not adapted when V_a is near zero). The blade motion is completely different between these two modes. Indeed for epicyloidal mode, the blade chord is roughly following the tangent of the main rotation (because V_r is higher than V_a), whereas for trochoidal mode the blade oscillates around the advance direction (as illustrated on Figures 1 and 2).

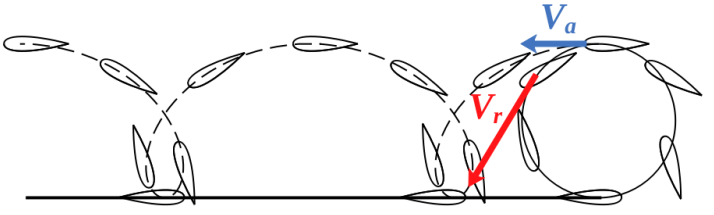

Figure 1: Epicycloidal path of a blade (from Fasse et al. (2022)).

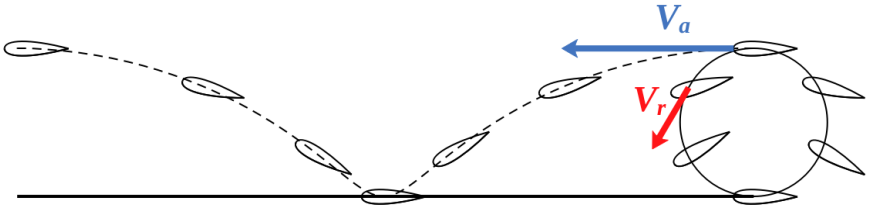

Figure 2: Trochoidal path of a blade (from Fasse et al. (2022)).

As an interesting marine propulsion system, cycloidal propeller have been studied by the IRENav with the development of a blade-controlled platform (Fasse et al., 2022). Thanks to an electrical blade-command design, this platform allows to reproduce blades' kinematic from all conceivable movements (trochoidal or epicycloidal kinematics). This electrical blade-command also allows authors to perform pitch law optimization to improve performances of current cycloidal propellers. The aim of this paper is to present an experimental optimization using a Gaussian process based method, coded by Sacher et al. (2017a), to maximize both thrust and efficiency of cycloidal propellers. The optimization uses experimental measurements collected from the instrumented blade-controlled platform. Experiments are performed at the Ifremer current tank. These experimental facilities are described in the first section as well as the parameterization of the pitch laws. The second section deals with the optimization method overview. Finally results of the optimization for λ=1.2 and λ=0.8 are given and compared to sinusoidal pitch laws for which results have previously been determined in Fasse et al. (2022). The gains obtained in terms of both thrust and efficiency for optimized pitch laws are discussed thanks to the analysis of experimental local blade force measurements.

2. Optimization Problem

2.1. Context

Cross-flow propeller generates a vectorial thrust which can be adapted in norm and direction. The main control parameter of this type of propulsion is the way the blades are moving through the incoming flow which is called the pitch law. The pitch law is therefore essential in the design performance of a cycloidal propeller and it is the purpose of the optimization process presented in this paper.

Most of existing cross-flow technologies use a mechanical system to operate the blade pitch motion. It is the case for the renowned Voith-Schneider Propeller (Schneider, 1928) for which blades are actuated by a rod/crank mechanism. More recently, Roesler et al. (2016) designed an experimental platform with a system of crankshaft and concentric collars to generate trochoidal motions and they performed measurements at the UNH testing facility in USA. The mechanical system implies a symmetrical blade pitch law to ensure the stability and the load balancing of the propeller. This is also the simplest way to design a mechanical cycloidal propeller. But due to the complexity of the flow and the strong disturbed wake, the blade behaviour has no reason to be symmetrical between up and downstream flow. Indeed during the upstream half-rotation, the flow viewed by the blades is undisturbed, whereas in the downstream half-rotation the blades encounter the wake of upstream other blades regularly disturbed by vortexes.

To deal with this challenge, authors choose to go through an experimental optimization of the cycloidal propeller pitch law using a non-symmetrical parameterization and an experimental platform able to operate this kind of laws.

2.2. Blade-controlled platform

To perform the optimization, the experimental blade controlled cross-flow propeller, called SHIVA developed by the authors, is operating at the Ifremer wave and current flume tank (characteristics of the tank are given by Gaurier et al. (2013)). Figure 3 gives an overview of the platform and its positioning at the flume tank. Thanks to a full electrical blade-control system, this platform can generate non-standard types of pitch laws.

SHIVA is composed of a triangular frame [F] in which three blades [I] are mounted. These blades are rotating thanks to three independent servo-motors [E] that gives them individual motions.

The outer frame [D] allows the platform to be elevated above the tank so that the blades are just below the waterline.

The design of the platform allow users to change the rotor diameter from 0.4 m to 0.8 m. The blade number N is fixed at 3. Each blade has a chord length $c = 0.15$ m and a span $l = 1$ m with a blade cross section of NACA 0018. For the presented measurements the diameter is fixed at $D = 0.4$ m and fiberglass-epoxy shells are used to increase the chord to $c = 0.35$ m to generate higher hydrodynamic loads. These dimensions lead to a solidity of the propeller $\sigma = 2.62$ (where the solidity is given by $\sigma = \frac{2Nc}{D}$).

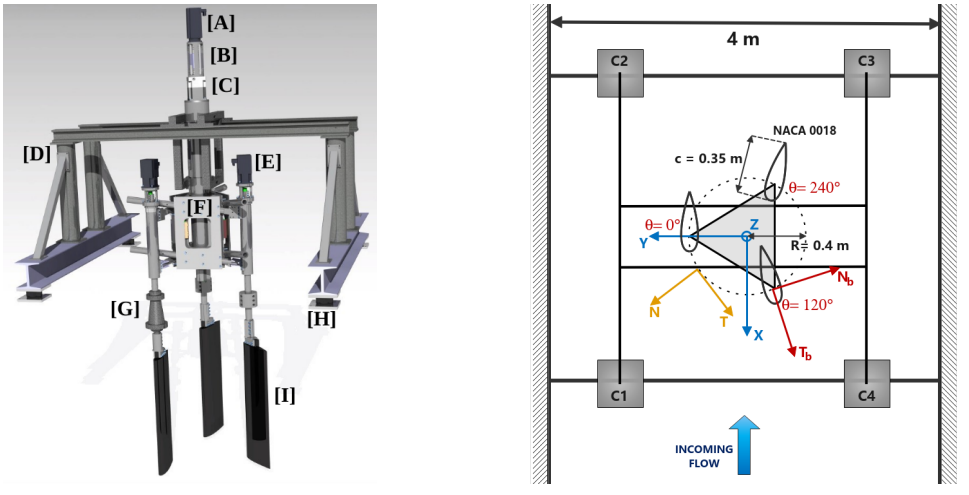

Figure 3: Blade-controlled platform and its positioning at the current flume tank.

The particularity of this experimental platform lies on the total electric blade pitch command. All the triangular frame is driven by the 2.5kW main motor [A] located at the top of the platform. A 50-ratio speed reducer [C] is used

to increase the torque and fits the rotational speed for the experiment values ($\sim$ 50 RPM). Each blade is independently actuated by a 0.8kW auxiliary motor [E]. The blades rotate around the quarter of their chord, close to the hydrodynamic center for the NACA 0018.

This rotation is called blade pitch and is referred to as the oriented angle φ between the tank flow direction (X-axis) and the blade chord (see Figure 5). The pitch angle can also be defined as the oriented angle β between the ortho-radial line of the main rotation and the blade chord. These two pitch angles are linked by the relation $\theta = \varphi - \beta$. The azimuth position of a blade θ is the position of its chord quarter on the main rotation disk (θ varies from 0° to 360°), and for an arbitrary time t_i, $\theta = \Omega t_i$ where Ω is the main rotational speed.

Expression of the pitch angle as a function of the azimuth position is the blade pitch law. The pitch law for blade 2 and blade 3 are $\frac{2\pi}{3}$ and $\frac{4\pi}{3}$ offset of those for blade 1. These laws are then tabulated as discrete functions on an embedded micro-controller unit which send regulation orders directly to the speed controllers for each blades in order to follow the reference pitch law. These laws are loaded on the platform via TCP/IP protocol (Ethernet) from a computer located alongside the tank. Pitch law can be loaded even during the rotation which helps to gain precious time during optimization procedure.

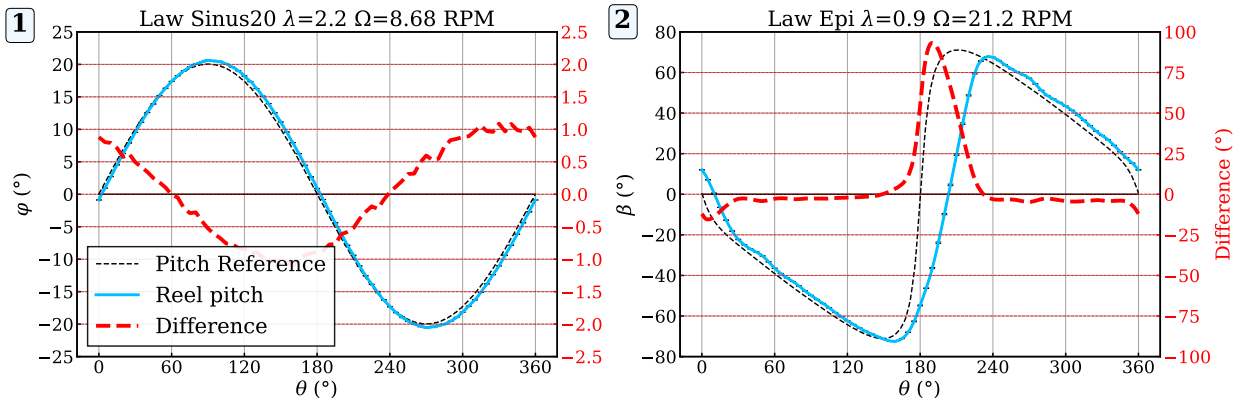

Figure 4: Pitch tracking for two different laws: 1) 20-Sinusoidal law in trochoidal mode (λ=2.2, V=0.8 m/s, Ω=8.68 RPM) and 2) Epicycloidal law (λ=0.9, V=0.8 m/s, Ω=21.2 RPM). Left axis refers to pitch angle in degrees(φ for trocho mode and β for epi mode) whereas right axis refers to the difference in degrees between real and reference pitch.

Because the pitch motion is electric and no more mechanical, a delay of the real blade position can occur when the motors can't follow the reference pitch according to their limits in speed and torque. Figures 4 gives an example of the pitch tracking for two laws: a trochoidal law at the left and an epicycloidal law at the right. These pitch tracking measurements have been performed during in water experiments with a tank speed V=0.8 m/s and a rotational speed Ω set for the desired λ value (Ω=8.68 RPM corresponding to λ=2.2 and Ω=21.2 RPM corresponding to λ=0.9). The pitch law for trochoidal mode (left) is given by the φ angle (pitch around the advance speed direction) whereas the pitch is expressed by β angle in epicycloidal mode (pitch around the tangent of the main rotation). The left axis (in red) of each sub-figure gives the difference between the reference sent to the blade engines and the real pitch experimentally measured. These results show that for trochoidal mode a maximal error of 1° occurs when the gradient ($d\varphi/d\theta$) is the highest. For epicycloidal mode, there is a blade reversal at θ=180°, which characterizes epicycloid motions. This quick motion is not well followed by the motors because of the speed limits (the error reaches almost 100°). After this huge error, the blade keeps a delay which is never caught. A detailed study of the pitch tracking error is given by Fasse et al. (2022).

In the present work, only trochoidal laws are performed on the SHIVA platform during experiments.

In addition, SHIVA is widely instrumented to measure time-dependant hydrodynamic loads and blade angular positions. Rotary incremental encoders provide angular position of each blade with a precision of 0.088° used simultaneously for the control loop as feedback and for loads measurements as projection angle. The azimuth position is also recorded by a rotary incremental encoders with a precision of 0.014°.

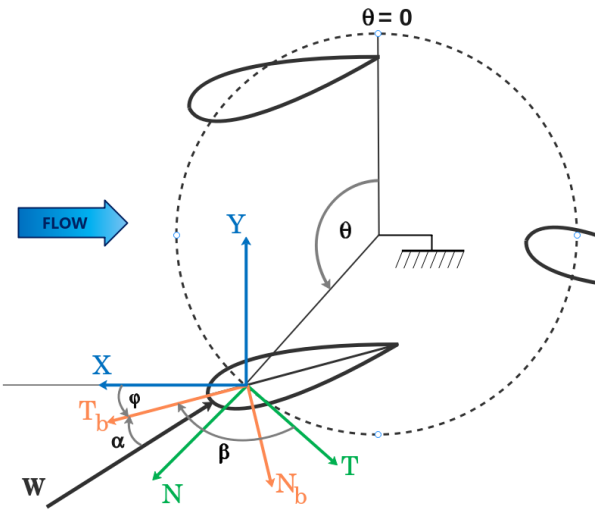

Figure 5: Representation of angles for an arbitrary position θ and an arbitrary relative velocity W (from Fasse et al. (2022)).

One blade is instrumented with an embedded 5-components load-cell [G] which measure local hydrodynamic loads in the direction of the blade's chord $\mathbf{T_b}$ (measuring range of 200 N) and normal to the blade $\mathbf{N_b}$ (measuring range of 900 N). This load-cell also measures the hydrodynamic torque $\mathbf{C_b}$ applied on the blade by hydrodynamic loads (measuring range of 60 Nm).
Four fixed 3-components load-cell [H] located between the outer frame I-beams and the tank I-beams provide global solicitations of the propeller in the X,Y and Z directions (measuring range of 5000 N in the X and Y direction and 7000 N for the Z direction). At least, a torque sensor [B] is installed between the main motor and the speed reducer and measures the torque applied on the main driveshaft (measuring range of 20 Nm).
Due to the wider measuring range of these fixed load-cell, in comparison with the embedded load-cell, post-processing of the loads is done with local hydrodynamic loads. The embedded load-cell measures temporal voltages, which are highly disturbed by high frequencies of electromagnetic environment. This is mainly due to the Pulse Width Modulation of speed controllers. Low-pass filter (35Hz cut-frequency) is thus applied on temporal signals. Then voltages are converted into loads thanks to the transfer matrix determined by in-house calibration. Finally, forces in blade coordinates ($\mathbf{F_{N_b}}$, $\mathbf{F_{T_b}}$) are projected into rotor coordinates ($\mathbf{F_N}$, $\mathbf{F_T}$) and absolute coordinates ($\mathbf{F_X}$, $\mathbf{F_Y}$) by Eq. (2) and (3) and illustrated in Figure 5.

$$\begin{pmatrix} \mathbf{F_T} \\ \mathbf{F_N} \end{pmatrix} = \begin{pmatrix} \cos(\beta) & -\sin(\beta) \\ -\sin(\beta) & -\cos(\beta) \end{pmatrix} \begin{pmatrix} \mathbf{F_{T_b}} \\ \mathbf{F_{N_b}} \end{pmatrix} \tag{2}$$

$$\begin{pmatrix} \mathbf{F_X} \\ \mathbf{F_Y} \end{pmatrix} = \begin{pmatrix} \cos(\theta) & \sin(\theta) \\ -\sin(\theta) & \cos(\theta) \end{pmatrix} \begin{pmatrix} \mathbf{F_T} \\ \mathbf{F_N} \end{pmatrix} \tag{3}$$

Then instantaneous forces are phase-averaged over one revolution, shifted of $\frac{\pi}{3}$ and $\frac{2\pi}{3}$, and summed to give the total force acting on the three blades. Lastly, total thrust coefficient and hydrodynamic efficiency are calculated as the non-dimensional averaged values:

$$\overline{C_{F_x}} = \frac{\overline{F_{x_{tot}}}}{0.5\rho S V^2} \qquad \eta = \frac{\overline{F_{x_{tot}}}\, V}{\overline{C_{tot}}\, \Omega} \tag{4}$$

Where $\overline{F_{x_{tot}}}$ and $\overline{C_{tot}}$ are respectively the mean of total thrust and total torque (measured on the main torque sensor) over 360°, S is the swept frontal area ($S = Dl$) and V the flume tank flow velocity.
These two performance definitions are used during the optimization process to evaluate the multi-objective function.

A more detailed description of the platform, its instrumentation and the blade control system, is given by Fasse et al. (2022). Only the embedded load-cell has been changed for a finer measuring range in the present paper (range of 900N and 200N respectively for F_{N_b} and F_{T_b} instead of 5000N and 1000N).

2.3. Parametric model

To proceed the optimization resolution, the first step is to develop an efficient parameterization. Indeed, Efficient Global Optimization methods, used here, allows to decrease the number of optimization evaluations of the objective function in comparison with genetic approaches. But the more the number of parameters is high and the more the number of optimization evaluations is required. In the present work, the number of parameters is 3.
The method presented in this paper (inspired from Abbaszadeh et al. (2019)) consists in defining the pitch law by a B-spline of degree 3 passing through four control points which are given by the 3 parameters $\mathbf{x_2}$ $\mathbf{x_2}$ and $\mathbf{x_2}$. Figure 6 illustrates the parameterization for two examples of random laws.

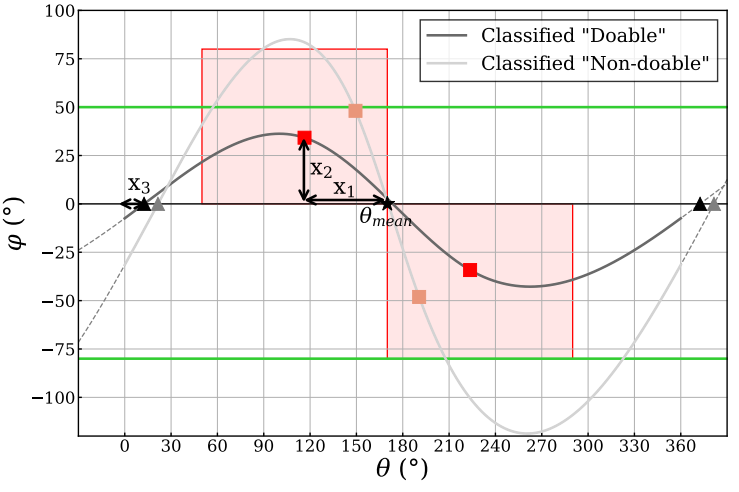

Figure 6: Parameterization method of the pitching law: red areas correspond to variability domain of parameters and green lines correspond to limits of maximal amplitude in absolute terms of parameterized laws.

The four control points of the spline are the two central red squares and the two extremities black triangles. These four control points can move thanks to the three following parameters:

- $\mathbf{x_1}$ and $\mathbf{x_2}$ parameters give the abscissa and the ordinate of the two central red squares: $\mathbf{x_1}$ is the distance between the red square abscissa and the central position θ_{mean}, whereas $\mathbf{x_2}$ is directly its ordinate. The second red square is constructed by central symmetry from θ_{mean}. For the presented results, the central position θ_{mean} is set at 170°. This central position involves a non-symmetrical pitch law which is the intent of this optimization as explained previously (the value 170° is fixed arbitrary).

- The third parameter $\mathbf{x_3}$ set the abscissa of the two extremities black triangles (the last black triangle is the 2π-offset of the first one). Their ordinates are fixed at zero. This last parameter deals with the offset of the law for the φ=0° crossing at the beginning and the end of the B-spline.

Each parameter can vary through the following ranges: $\Delta x_1 = [0.5 : 120]$, $\Delta x_2 = [0.5 : 80]$, $\Delta x_3 = [-5 : 40]$. Variations of $\mathbf{x_1}$ and $\mathbf{x_2}$ lead to the shift of the two central red squares within the two red areas, that are shown in Figure 6. These variables have two main effects on the pitching law: the amplitude shift and the dissymetrization of the law. The variation of the $\mathbf{x_3}$ leads to the shift of the two extremities black triangle and has the effect of controlling the pitch angle (possibly non-zero) at the beginning of the law. The three ranges $\Delta x_{1,2,3}$ are also defining the optimization domain, also called parametric space.
This method of parameterization implies a weakness which occurs when two points of the spline are to close, the amplitude of the spline can be very high and the slope close to the infinity. Another approach would be to define the spline with 4 parameters, in order to directly control in amplitude and azimuthal position the extrema of the spline,

where the derivative would be imposed as zero. However, an optimization process of 4 parameters requires more evaluations of the objective function and much more solving time considering experimental evaluation.
In order to be able to dissymmetrize the law, using only 3 variables, a classification method (Sacher et al., 2018b) is implemented during the optimization procedure (see details in Section 3.2).

The classification method consists on defining two limits (high and low) of the spline and classify the parameterized spline "doable" if all the points of the spline are between these two limits. These limits are represented in green on Figure 6 and fixed at $\varphi = 50°$ and $\varphi = -80°$ for the present experiments. These limits have also been chosen to restrict the acceleration between the two halves of the pitching law to deal with the auxiliary engine acceleration limits. Indeed, if the slope of the pitching curve is to high, the auxiliary engine will not follow correctly the reference because the pitch velocity is too high and a large delay will occur. A classification meta-model is initially built from a large number (400 in this work) of candidate laws that are not measured in the water tank, but that are tagged with 'doable' or 'not doable' spec. This meta-model then gives access to the prediction that a new law (parameterized by the variables x_1, x_2 and x_3) belongs to one of these two classes. This prediction is given in the form of a probability $P(\boldsymbol{x}) \in [0,1]$, which has the main advantage of being a continuous function in the space of variables, and avoids the selection of new 'not doable' laws in the optimization process (Sacher et al., 2018b).

3. Multi-objective Surrogate-based Optimization

We consider abstract optimization problems, where several objectives have to be minimized simultaneously over a design variable $\Omega \subset \mathbb{R}^d$:

$$\min_{\boldsymbol{x}\in\Omega} f_1(\boldsymbol{x}), \dots, f_m(\boldsymbol{x}) \quad \text{s.t.} \quad \boldsymbol{g}(\boldsymbol{x}) \leq 0 \tag{5}$$

where $\boldsymbol{x} = \left(x_i\right)_{1\leq i\leq d}$ is a vector of design variables, $\boldsymbol{f} = \left(f_j\right)_{1\leq j\leq m}$ is a vector of objective functions to be minimized $\left(f_i : \Omega \mapsto \mathbb{R}\right)$, and $\boldsymbol{g} = \left(g_k\right)_{1\leq k\leq p}$ is a vector of inequality constraints $\left(g_k : \Omega \mapsto \mathbb{R}\right)$. The existence of an optimal solution, minimizing all objectives at once is usually not granted. This leads to the search for an optimal set of solutions, called the Pareto front. According to the Pareto domination rule (Fonseca and Fleming, 1998), $\boldsymbol{x} \in \Omega$ is said dominated by $\boldsymbol{x'} \in \Omega$ if for all $1 \leq j \leq m$, $f_j\left(\boldsymbol{x'}\right) \leq f_j(\boldsymbol{x})$, and $\boldsymbol{g}\left(\boldsymbol{x'}\right) \leq 0$. The set of optimal (non-dominated) design vectors, to be determined in Ω, is then called the Pareto set. Evolutionary algorithms (Deb et al., 2002; Coello et al., 2007) have been shown to be well-adapted for solving multi-objective problems in real-word applications with moderate objective computation cost (Huang et al., 2015; Lim and Kim, 2019).

In the present work, individual evaluations of the objective functions are assumed to be very expensive. A common approach is then to use surrogate models in place of $\boldsymbol{f}$ to reduce the computational burden related to the evaluations of $\boldsymbol{f}$ (Simpson et al., 2001). Gaussian processes (GP) (Rasmussen and Williams, 2006; Kleijnen, 2009) are presently considered, which, owing to their statistical nature, provide for each objective function, both a prediction value and a measure of the uncertainty (variance) in this prediction. These features are appealing in the optimization context, as they can be exploited to derive rigorous optimization strategies, by evaluating sequentially the computer models at design vectors that maximize a so-called merit function (Picheny et al., 2013).

In mono-objective problems, GP-based approaches are globally referred to as Efficient Global Optimization (EGO) (Jones et al., 1998), where the merit function is based on an Expected Improvement (EI) criterion, expressing a trade-off between sampling in promising regions and exploring in unsampled regions. EGO has been successfully applied to complex optimization problems, such as non-linear fluid-structure interaction problems (Sacher et al., 2017b, 2018a) or RANS computations (Meliani et al., 2019).

Over the last few years, surrogate-based approaches have also been proposed to address the multi-objective problem. Indeed, several GP-based multi-objective optimization strategies propose to extend the EI infilling criterion of Jones et al. (1998). The definition of the improvement can then be considered over the Pareto front (Wagner et al., 2010), using for instance, Maximin distance (Svenson and Santner, 2010), Euclidean distance (Keane, 2006), or the well-known Hypervolume infilling criterion (Emmerich et al., 2006, 2011; Luo et al., 2014). Recently, merit functions aimed at computing and reducing uncertainty of the predicted Pareto front have been developed (Picheny, 2015; Binois et al., 2015; Passos and Luersen, 2018). In particular, Passos and Luersen (2018) have proposed and validated, on a real-word composite panel application, the efficiency of a new merit function: Minimization of the Variance of the Predicted Front (MVPF).

In the present work, the MVPF approach is applied in combination with the Expected Improvement Matrix Hypervolume (EIMH) (Zhan et al., 2017) criterion, to solve the blade pitch law optimization problem.

In Section 3.1, we summarize the construction of a GP model for an objective function f_j. Definitions of multi-objective surrogate-based merit functions, that are used in the present optimization under non-doable observations, are then provided in Section 3.2.

3.1. GP surrogate construction

In the present Section 3.1, the GP surrogate construction of an objective function f_j is provided. The method is exactly the same for the GP surrogate construction of an inequality constraint function g_k.

We consider a set of n training points $\mathcal{X} = \left(\boldsymbol{x}_1, \dots, \boldsymbol{x}_n\right)$, each in Ω. The training points are associated to the vector $\mathcal{Y}^{(j)} = (y_1^{(j)}, \dots, y_n^{(j)})$ of noisy observations of the objective function f_j. It is assumed that $y_i^{(j)} = f_j(\boldsymbol{x}_i) + \epsilon_i^{(j)}$, where the $\epsilon_i^{(j)}$ are independent and identically distributed Gaussian random variables having zero-mean and variance $\sigma_{\epsilon_j}^2$.

The GP construction considers that $f_j(\boldsymbol{x})$ is a realization of a zero-mean multivariate Gaussian process with covariance function C_j. We consider here the multidimensional squared exponential covariance functions defined by

$$C_j\left(\boldsymbol{x},\boldsymbol{x}';\Theta_j\right) \doteq \theta_1 \prod_{i=1}^{d} \exp\left(\frac{-\left(x_i - x_i'\right)^2}{2l_i^2}\right) + \theta_2 \tag{6}$$

where $\Theta_j = \left(\theta_1^{(j)}, \theta_2^{(j)}, l_1^{(j)}, \dots, l_d^{(j)}\right)$ is the vector of covariance hyper-parameters to be inferred from the $\mathcal{Y}^{(j)}$ observations. From the conditional rules of joint Gaussian distributions (Rasmussen and Williams, 2006), the *best* prediction $\widehat{f}_j(\boldsymbol{x})$ of $f_j(\boldsymbol{x})$, *i.e.* the mean of $y^{(j)}$, and the prediction variance $\widehat{\sigma_j}^2(\boldsymbol{x})$ are given by,

$$\widehat{f}_j(\boldsymbol{x}) = \boldsymbol{k}_j^{\mathrm{T}}(\boldsymbol{x}) \left(\boldsymbol{C}_j\left(\Theta_j\right) + \sigma_{\epsilon_j}^2 \boldsymbol{I}\right)^{-1} \mathcal{Y}^{(j)} \tag{7}$$

$$\widehat{\sigma_j}^2(\boldsymbol{x}) = \kappa_j(\boldsymbol{x}) + \sigma_{\epsilon_j}^2 - \boldsymbol{k}_j^{\mathrm{T}}(\boldsymbol{x}) \left(\boldsymbol{C}_j\left(\Theta_j\right) + \sigma_{\epsilon_j}^2 \boldsymbol{I}\right)^{-1} \boldsymbol{k}_j(\boldsymbol{x}) \tag{8}$$

In (7) and (8) we have denoted $\boldsymbol{C}_j \in \mathbb{R}^{n \times n}$ the symmetric covariance matrix of the training points, $\kappa_j(\boldsymbol{x}) \doteq C_j\left(\boldsymbol{x},\boldsymbol{x};\Theta_j\right)$, $\boldsymbol{k}_j(\boldsymbol{x}) \doteq \left(C_j\left(\boldsymbol{x},\boldsymbol{x}_1;\Theta_j\right) \cdots C_j\left(\boldsymbol{x},\boldsymbol{x}_n;\Theta_j\right)\right)^{\mathrm{T}}$ the covariance vector between the observations in $\mathcal{X}$ and $\boldsymbol{x}$, and $\boldsymbol{I}$ the identity matrix of $\mathbb{R}^n$. The hyper-parameters Θ_j and noise variance $\sigma_{\epsilon_j}^2$ can be determined by maximizing the log-marginal likelihood (see Rasmussen and Williams (2006) for more details).

3.2. Merit functions under non-doable design vectors

Surrogate-based optimization methods rely on the sequential construction of statistical surrogate models, using training sets of computed objective and constraint function values, that are refined according to a prescribed infilling strategy (i.e. merit functions (Picheny et al., 2013)). At each iteration of the iterative surrogate-based optimization, a new design vector $\boldsymbol{x}_{n+1}$ is thus added to $\mathcal{X}$, and finally $\boldsymbol{f}$ and $\boldsymbol{g}$ are computed. A new iteration can then start by updating surrogate models, and the iterative process is repeated until a stopping criterion is satisfied or the resources allocated to the optimization have been exhausted.

In real world applications, however, this sequential optimization procedure may stop prematurely if an objective function cannot be computed at a proposed $\boldsymbol{x}_{n+1}$. Indeed, such a situation may occur when the search space encompasses design points corresponding to a non-physical configuration or an ill-posed problem, for example. Sacher et al. (2018b) have proposed to use a classification model to learn non-doable design vector areas alongside the surrogate-based optimization and adapt the infilling strategy accordingly. In short, a probabilistic classification model is built using the union of doable and non-doable training sets. The classifier is then incorporated in the surrogate-based optimization procedure to avoid proposing new design vectors in the non-doable domain while improving the classification uncertainty if needed.

In the present work, two new design vectors are determined under the constraint to be in the doable domain and added to $\mathcal{X}$ at each new iteration of the iterative surrogate-based optimization. Specifically, the MVPF and EIMH criteria are considered (see next Sections 3.2.1 and 3.2.2) to allow respectively, the reduction of the uncertainty of the predicted Pareto front and the improvement of the computed Pareto front.

3.2.1. Minimization of the Variance of the Predicted Front (MVPF)

The MVPF infilling criterion, proposed by Passos and Luersen (2018), aims at improving the fidelity of the predicted Pareto front. A Pareto front is generated thanks to a state-of-the-art multi-objective constrained optimization algorithm (such as NSGA-II (Deb et al., 2002)) and using GP surrogate predictions (one for each objective and constraint function, see Eq. (7)) as input functions. The MVPF criterion then consists of selecting a design vector variable $\boldsymbol{x}_{MVPF}$ from the Pareto set $\mathcal{X}_{PF}$, to be evaluated. This selection is based on the highest predicted variances in objective functions (see Eq. (8)), and is written as,

$$\boldsymbol{x}_{MVPF} \doteq \underset{\boldsymbol{x}\in\mathcal{X}_{PF}}{\arg\max}\left(\prod_{j=1}^{m} \underline{\widehat{\sigma}_j^{\,2}}(\boldsymbol{x})\right) \tag{9}$$

where $\underline{\widehat{\sigma}_j^{\,2}}(\boldsymbol{x}) \in [0,1]$ is the normalized (from Pareto set) predicted variance. For more details on the MVPF criterion, we refer readers to (Passos and Luersen, 2018).

3.2.2. Expected Improvement Matrix Hypervolume criterion (EIMH)

Multi-objective EI criteria have usually similar processes, where in first, an improvement function over the Pareto front is defined. In second, the expected value of the improvement function is computed by integrating it over the non-dominated region. Zhan et al. (2017) have proposed the concept of Expected Improvement Matrix (EIM) to address the usage of multi-objective EI criteria in real world applications, especially when dealing with many objective problems. This EIM concept uses a combination of $t \times m$ simple 1-D integrations to compute a cheap-to-evaluate and still efficient multi-objective EI (t is the number of non-dominated design vectors and m is the number of objectives). In (Zhan et al., 2017), the scalar Expected Improvement function $EI(\boldsymbol{x})$ is expanded into a 2-D matrix EIM, in which,

$$EI_j^q(\boldsymbol{x}) \doteq \left(f_j^q - \widehat{f}_j(\boldsymbol{x})\right)\Phi\left(\frac{f_j^q - \widehat{f}_j(\boldsymbol{x})}{\widehat{\sigma}_j^{\,2}(\boldsymbol{x})}\right) + \widehat{\sigma}_j^{\,2}(\boldsymbol{x})\phi\left(\frac{f_j^q - \widehat{f}_j(\boldsymbol{x})}{\widehat{\sigma}_j^{\,2}(\boldsymbol{x})}\right) \tag{10}$$

where $j = 1, \ldots, m$ and $q = 1, \ldots, t$. The element $EI_j^q(\boldsymbol{x})$, in EIM, corresponds to the EI of the studying point $\boldsymbol{x}$ beyond the qth non-dominated front point in the jth objective. From the EIM matrix, Zhan et al. (2017) have then proposed three infilling criteria (Euclidean distance, Maximin distance and Hypervolume improvement) to aggregate the EIM into a scalar value to measure the overall improvement of the studying point compared against the Pareto front. In the present work, the Hypervolume-based EIM criterion is applied, leading to the selection of a design vector variable $\boldsymbol{x}_{EIMH}$. For more details on the EIMH criterion, interested readers are refereed to (Zhan et al., 2017).

3.2.3. Median Compromise of the Pareto Front (MCPF)

Solving multi-objective optimization problems leads to the search of the optimal set of solutions (i.e. Pareto front). In most real-word applications, a design vector from the Pareto set has to be selected to provide an optimal design choice. This selection is thus a compromise choice, which is usually based on the knowledge of the designer. With the aim of avoiding this designer compromise selection, the MCPF criterion is used in the present work, and is given by,

$$\boldsymbol{x}_{MCPF} \doteq \underset{\boldsymbol{x}\in\mathcal{X}_{PF}}{\arg\min}\left(\sum_{j=1}^{m} \arg\operatorname{sort}\left(\widehat{\boldsymbol{f}}_{PF_j}, \widehat{f}_j(\boldsymbol{x})\right)^2\right) \tag{11}$$

where, $\arg\operatorname{sort}(\boldsymbol{f}, f) \doteq \left\{q \in \{1, \ldots, t\} \mid f < f_q \in \boldsymbol{f}\right\}$ and $\widehat{\boldsymbol{f}}_{PF_j}$ is the vector of objective function j predictions on the Pareto set $\mathcal{X}_{PF}$, which is composed of t non-dominated design vectors. As can be seen in Eq. (11), the median trade-off is selected by considering the rank, from the Pareto set, of each objective function prediction. This definition allows a design vector compromise to be determined without the need for weights or scaling of objective function.

4. Results and Discussion

Two experimental optimizations have been carried out for two different values of λ for which experimental conditions are the following:

- λ=1.2, V=0.8 m/s, Ω=15.92 RPM
- λ=0.8, V=0.6 m/s, Ω=17.90 RPM

Approximately 50 optimization steps have been performed during 8 hours of experiments for each optimization cases. The tank speed have been reduced for the optimization at λ=0.8 to avoid sensor saturation problems due to the increase in main rotational speed.

Figure 7 gives meta-models representation in 3d parametric space at the end of optimization for λ=1.2 (for λ=0.8, the meta-models are close in terms of optimum location and bring no added value). The meta-model for the thrust is drawn at the left and those for the efficiency is drawn at the right. Octahedrons are the experimental points located into the optimization domain as functions of the parameters which were used to generated the parameterized pitch law. As mentioned earlier, all experimental points are inside the front area delimited by the black 50%-probability iso-surface of classification. Octahedrons are colored with their objective value (total thrust coefficient at the left and efficiency at the right). Slices show the meta-model predictions, colored as functions of the optimization objectives. Lastly, for respectively the thrust and the efficiency, the red iso-surface represents the areas of the meta-model where the thrust coefficient is higher than 0.75 and respectively higher than 0.63 for the efficiency.
Results show that depending on the objective function (thrust or efficiency maximizing), the optimums are not located on the same area and thus the optimized pitch law is slightly different from one objective to the other one.

	$\lambda = 1.2$					$\lambda = 0.8$				
Pitch laws	x_1	x_2	x_3	$\overline{C_{F_X}}$	η	x_1	x_2	x_3	$\overline{C_{F_X}}$	η
$CF_{x_{optim}}$	49.58	8.08	38.65	0.774	0.524	25.50	8.1	22.43	1.37	0.370
η_{optim}	62.24	20.37	18.02	0.521	0.643	27.84	17.73	9.27	1.10	0.573
Best_compromise	34.58	8.51	22.73	0.728	0.562	27.19	12.26	29.50	1.31	0.439
Sinus10	-	-	-	0.670	0.485	-	-	-	1.17	0.267
Sinus20	-	-	-	0.465	0.570	-	-	-	1.11	0.398
Sinus30	-	-	-	0.189	0.465	-	-	-	0.792	0.420

Table 1
Main experimental results of both optimization and comparison with sinusoidal pitch laws results.

Figure 8 presents the optimized pitch laws obtained at the end of the optimization. For both λ cases (λ=1.2 at the left and λ=0.8 at the right), the three following optimized laws are plotted:

- CFx_{optim} which presents the best thrust coefficient
- η_{optim}: which presents the best hydrodynamic efficiency
- $Best\_compromise$: which have the best rank of the MCPF criterion

The three parameters for these resulting optimized pitch laws are summed up in Table 1. As it can be seen, for both λ cases, the law which maximizes the thrust has a lower maximal amplitude (around 10°) than the law which maximizes the efficiency (above 20°). As might be expected, the law with the best compromise is located just between the two others. With the diminution of the λ parameter, same observations are noticed with yet a 10°-increase of the maximal amplitude. This result is consistent with previous measurements from Fasse et al. (2022) on sinusoidal pitch laws for which the more λ is high the more the maximal amplitude decrease to obtain the best hydrodynamic performances.

These investigations about the shape of optimized pitch laws lead to look after the Pareto front of the compromise thrust/efficiency which is illustrated in the Figure 8 (center). Points are plotted as functions of their thrust coefficient values (X coordinate) and efficiency (Y coordinate). Red squares correspond to the optimization done at λ=1.2 whereas blue triangles correspond to the λ=0.8 optimization. Small colored triangles and squares are the experimental results while single-colored medium ones correspond to predictions of the surrogates. Lastly, sinusoidal results, represented with larger lone markers, are given to compare them to the optimized laws. Sinusoidal laws have been performed for the same λ values than for the optimization (λ=1.2 for red squares and λ=0.8 for blue triangles) and with the same experimental conditions.

These Pareto fronts clearly show the gain for both efficiency and thrust in comparison with sinusoidal laws. The Table 1 summarizes main results of thrust coefficient and efficiency. The gains are mainly explained by the shape of

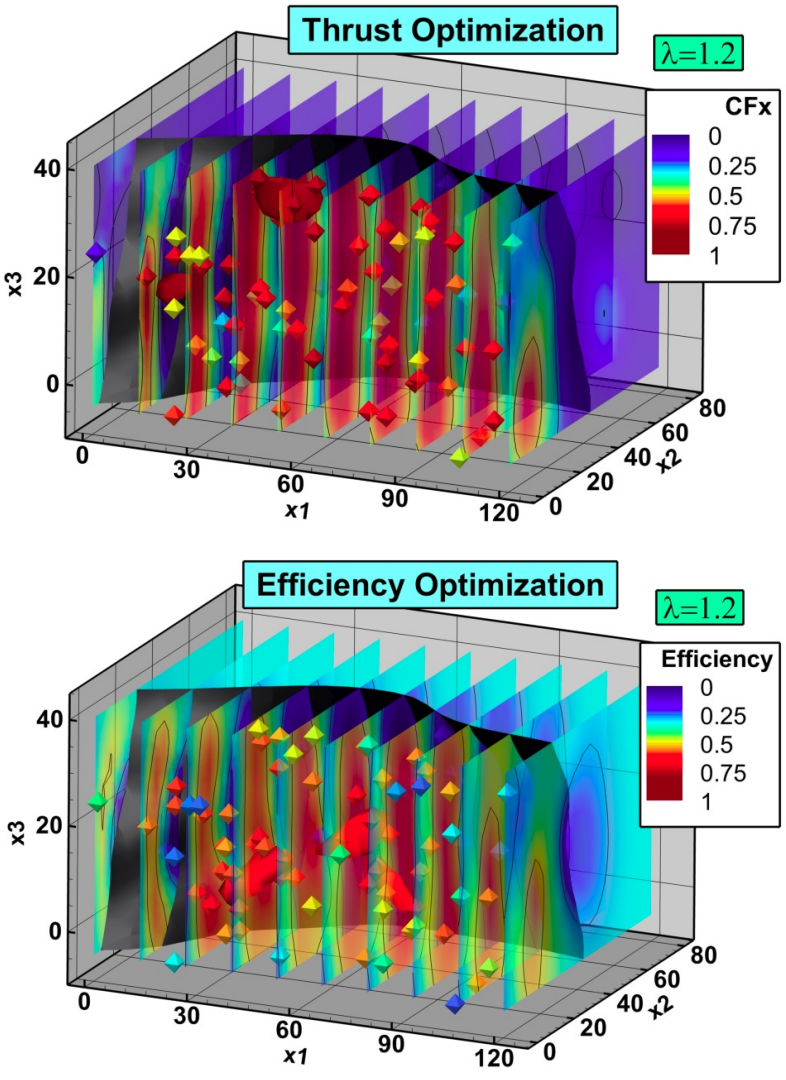

Figure 7: Meta-models for Thrust (left) and Efficiency (right) at the end of multi-objective optimization for λ=1.2.

the optimized pitch law. Optimized laws show a clear horizontal-offset of the law at the beginning which implies a negative pitch at θ=0° and during the first 30° of the rotation. A significant increase of the maximal amplitude during the downstream half rotation in comparison with the upstream one may also explain this gain. Lastly, this maximal amplitude is slightly shifted to θ=110° due to the dissymetry.

Figures 9 and 10 show the experimental blade forces during the whole rotation for the maximal thrust pitch law (CFx_{optim}) and the maximal efficiency pitch law (η_{optim}) for the two λ optimization cases. Upper sub-figures illustrate the experimental hydrodynamic force measured on one blade during one revolution whereas below sub-figures show the single-blade thrust coefficient (projection of the hydrodynamic force on the advance direction) and the tangential coefficient (projection of the hydrodynamic force on the main rotation tangent, which is an image of the main torque).

For the case λ=1.2, the CFx_{optim} pitch law (in red) is compared to the Sinus10 pitch law (in blue) which provides the best thrust coefficient for sinusoidal laws at λ=1.2 whereas the η_{optim} pitch law (in orange) is compared to the Sinus20 pitch law (in navy).
The horizontal offset of the pitch law (due to the parameter $\mathbf{x_3}$) at the beginning of the rotation (upstream half) has

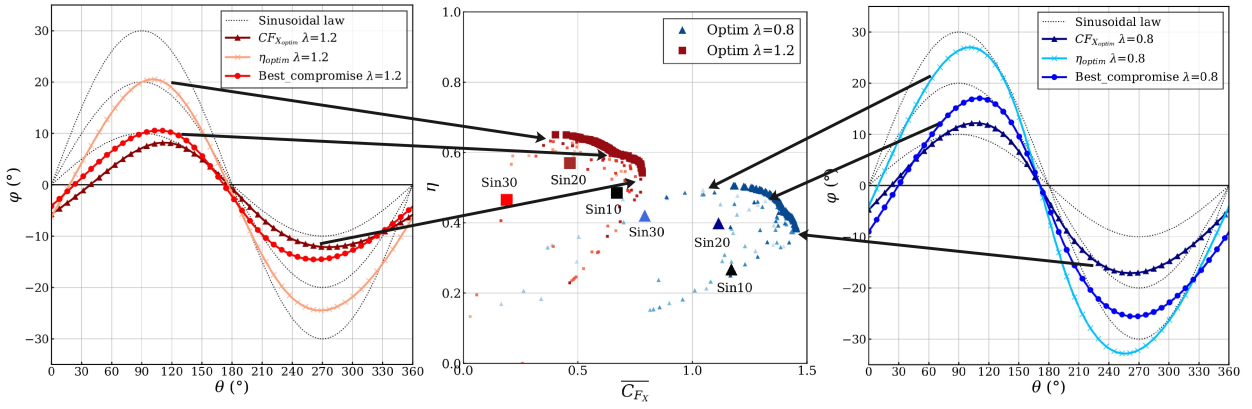

Figure 8: Comparison of the pitch laws obtained after optimization procedure for λ=1.2 (left) and λ=0.8 (right) and their resulting Pareto fronts (center).

the following effect: it induces an offset of the inversion of the hydrodynamic force direction against the main disk which occurs around θ=0° for both parameterized pitch law whereas it occurs around θ=30° for Sinus10 and θ=45° for Sinus20. That mainly implies an early generation of the hydrodynamic force in the advance direction for optimized pitch law in comparison with sinusoidal laws. This observation is reflected on the thrust coefficient signal which is higher for both CFx_{optim} and η_{optim} pitch laws between θ=30° and θ=100° than for sinusoidal laws. Thrust performance of CFx_{optim} and η_{optim} pitch laws are then higher than for the respective sinusoidal laws. The gain in total thrust coefficient of the CFx_{optim} law is 13.4% in comparison with the Sinus10 law and 10.7% for the η_{optim} law compare to the Sinus20 law. Lastly, to compare the two optimized law, CFx_{optim} shows a higher thrust peak in the downstream half than in upstream whereas η_{optim} for which the downstream thrust peak is smaller than the upstream peak. But this thrust increasing implies a increase of the tangent force coefficient which is negative (opposite to the rotation) so involves an higher main torque and so reduce the hydrodynamic effiency. For the η_{optim} law, the tangent force coefficient is very reduced on the downstream half in comparison with the other laws. That implies a efficiency gain of 11.3% in comparison with the Sinus20 law.

Figure 10 presents results for the case λ=0.8. The CFx_{optim} and η_{optim} pitch laws are respectively compared to the Sinus10 and Sinus30 which respectively provide the best thrust coefficient and the maximal efficiency at λ=0.8 for sinusoidal pitch laws. The hydrodynamic forces for this case are much larger than for the case λ=1.2, in part because of the increase of the relative velocity between λ=1.2 and λ=0.8. As observed for the λ=1.2 case, optimized pitch laws (CFx_{optim} and η_{optim}) have the horizontal offset of the pitching law at the beginning of the rotation which involve a early production of the thrust. The gain in thrust is significant for both upstream and downstream halves. The CFx_{optim} law for λ=0.8 shows a 14.6% gain on the total thrust coefficient in comparison with the Sinus10 pitch law. For the η_{optim} law, the gain is remarkable on the efficiency with a gain on the thrust and a decrease of the tangential force in comparison with the Sinus30. It leads to a 26.7% gain on the hydrodynamic efficiency.

The greater gains obtained with parameterized pitch laws at λ=0.8 are explained by the fact that sinusoidal laws are adapted for trochoid mode (λ>1) and far less adapted for epicycloid mode. Parameterized laws therefore allow to exceed sinusoidal law performances in starting phase.

The two distinct fronts also highlight that for each λ parameter the compromise is different: for λ=1.2 the best compromise leads to a better efficiency whereas for λ=0.8 it leads to a higher thrust. This motivates the generalization of the optimization procedure for other λ values to have a large set of optimized pitch laws for a wide range of advance speeds and operation configurations.

The objective function of the optimization can also be reconsidered. Indeed for propulsion purpose, the search of the best efficiency for a given value of thrust is more appropriate. Knowing the hull resistance (depending on the shape and dimensions of the hull) as well as the required advance speed, the pitch law which provides the sufficient thrust to overcome hull resistance and with the best efficiency can be determined with this optimization procedure.

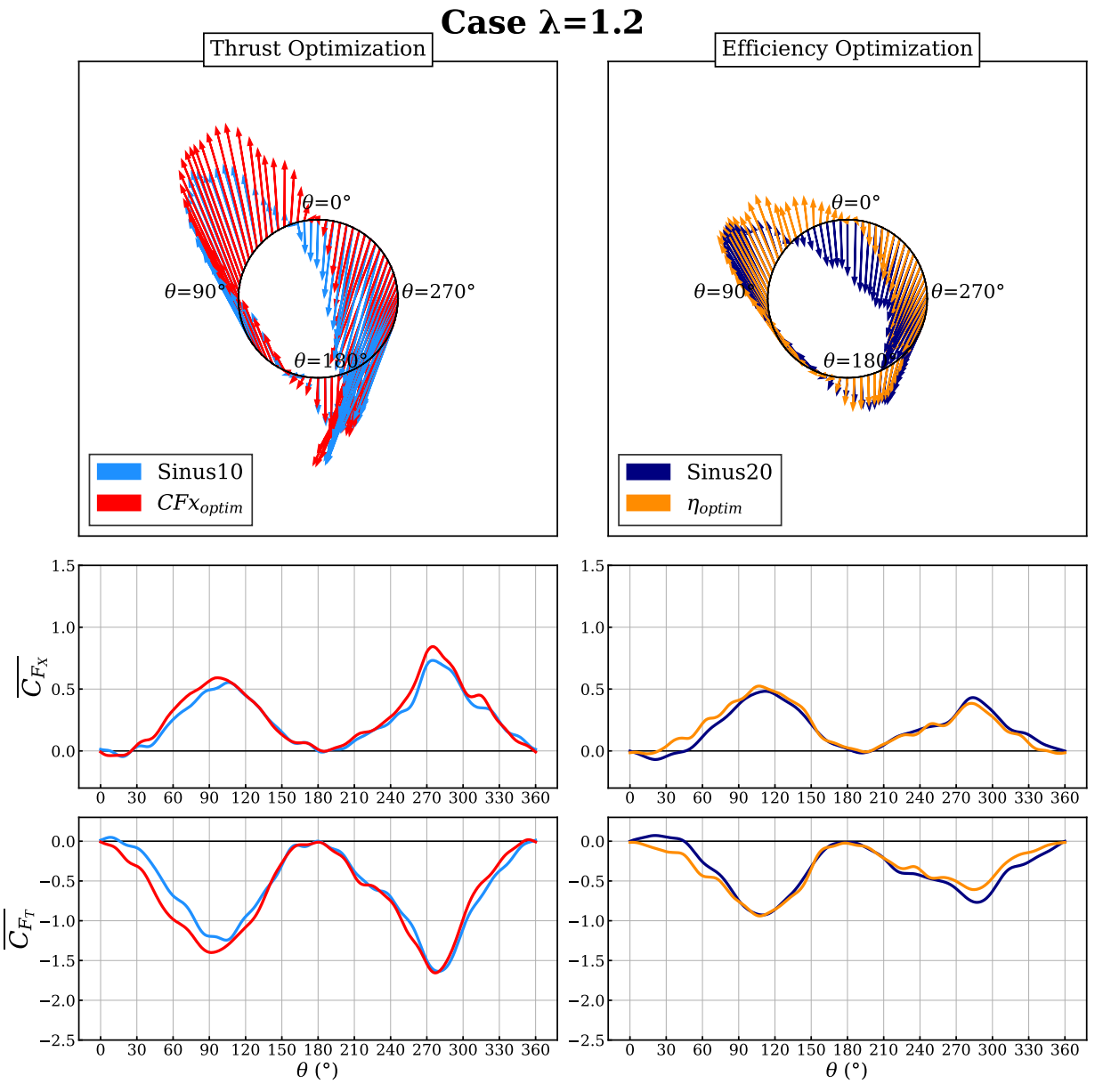

Figure 9: Results of thrust force and tangential force for the law maximizing the thrust (left) and maximizing efficiency (right) for the case λ=1.2 and comparison with sinusoidal laws.

5. Conclusion

This paper presents an experimental optimization of a cycloidal propeller blade pitch laws. Indeed, for this specific type of propulsion, characterized by the rotation of blades around an axis perpendicular to the ship advance speed, the blade motion has a huge impact on the propeller performances. Traditional cycloidal propellers have a mechanical system which deals with the blade pitch rotation. These systems, represented by sinusoidal pitch law in trochoidal mode (λ >1 systems), show limitations in term of efficiency. A fully electric system, as the SHIVA platform described in this paper, can surpass the performances by managing non-symmetrical blade pitch laws.

By using a suitable parameterization of the pitch laws allowing a wide diversity of pitch motion, the multi-objective optimization is performed on experimental measurements of the SHIVA platform at the Ifremer current tank. Results

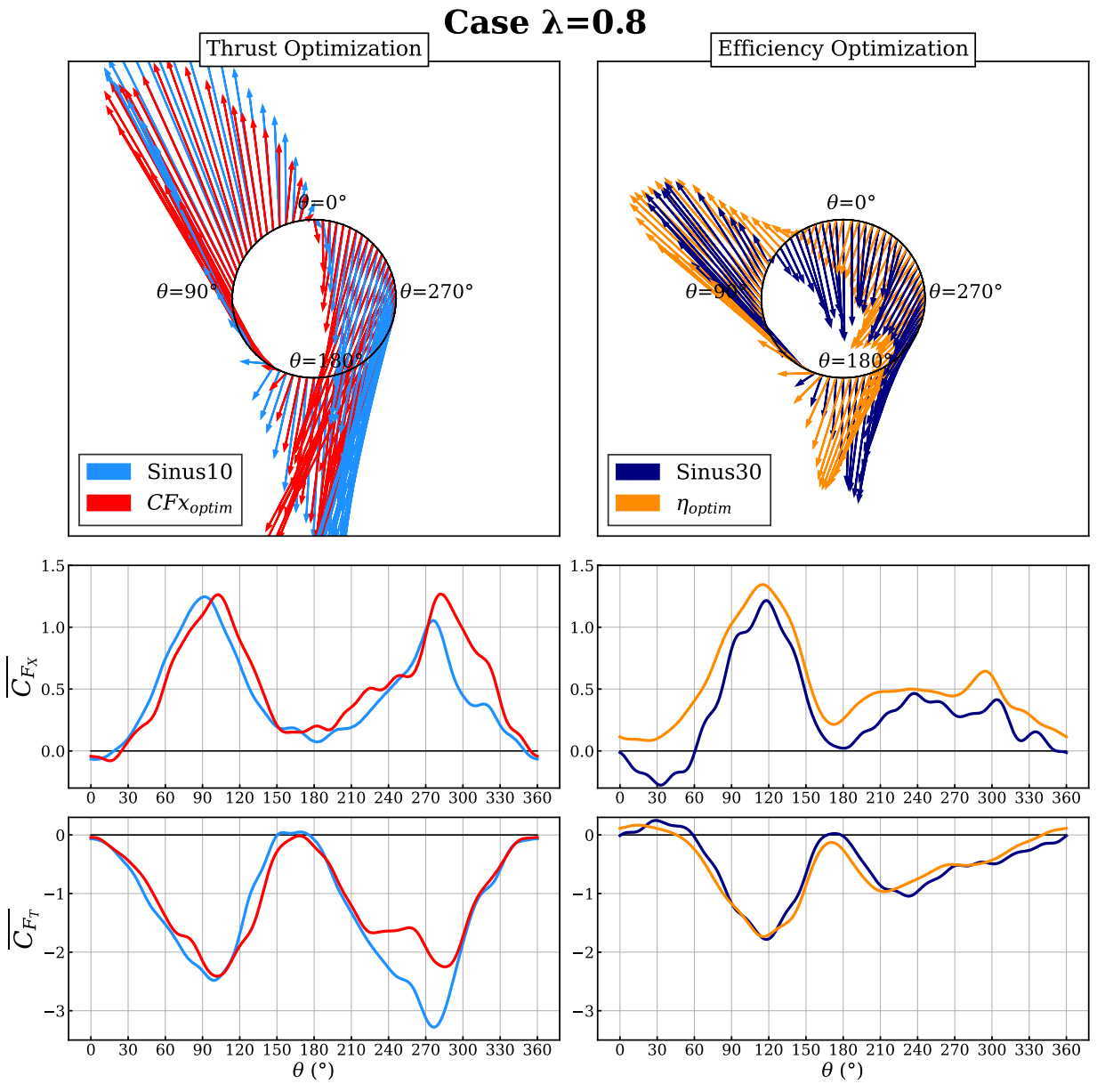

Figure 10: Results of thrust force and tangential force for the law maximizing the thrust (left) and maximizing efficiency (right) for the case λ=0.8 and comparison with sinusoidal laws.

shows that a trade-off is necessary concerning the pitch law shape to maximize the thrust or the efficiency. A Pareto front is thus determined between these two objectives to search for the best compromise law. The results and the comparison with sinusoidal results show a significant improvement of both thrust and efficiency with gains of respectively 13.4% and 11.3% at λ=1.2 and respectively 14.6% and 26.7% at λ=0.8.

Finally, because experimental optimization takes time, the procedure have been carried out for only two λ values. As perspectives, it will be interesting to repeat this optimization for a range of λ values to compare the performances of the cycloidal propeller for many operating points. The same optimization procedure could be reproduce for epicycloid mode with a parameterization of the pitch angle β whereas the pitch angle φ.

The study of the objective function is also important. For propulsion purpose, the main goal is to maximize the

efficiency for a given total thrust force (which surpass the hull resistance). The same optimization could therefore be proceed with a constraint on the thrust force for a given hull shape and dimension.
An other perspective is to upgrade the SHIVA platform with the installation of a Artificial Intelligence to deal with the automatizing of the optimization. Indeed, here the optimization is performed step by step during long measurements. But thanks to its embedded instrumentation, the platform could process an automatic optimization for various advance speeds and adapt the pitching law for various objectives.

References

Abbaszadeh, S., Hoerner, S., Maître, T., Leidhold, R., 2019. Experimental investigation of an optimised pitch control for a vertical-axis turbine. IET Renewable Power Generation 13, 3106–3112.

Binois, M., Ginsbourger, D., Roustant, O., 2015. Quantifying uncertainty on pareto fronts with gaussian process conditional simulations. European journal of operational research 243, 386–394.

Coello, C.A.C., Lamont, G.B., Van Veldhuizen, D.A., et al., 2007. Evolutionary algorithms for solving multi-objective problems. volume 5. Springer.

Deb, K., Pratap, A., Agarwal, S., Meyarivan, T., 2002. A fast and elitist multiobjective genetic algorithm: Nsga-ii. IEEE transactions on evolutionary computation 6, 182–197.

Doijode, P.S., Hickel, S., van Terwisga, T., Visser, K., 2022. A machine learning approach for propeller design and optimization: Part i. Applied Ocean Research 124, 103178.

Emmerich, M.T., Deutz, A.H., Klinkenberg, J.W., 2011. Hypervolume-based expected improvement: Monotonicity properties and exact computation, in: 2011 IEEE Congress of Evolutionary Computation (CEC), IEEE. pp. 2147–2154.

Emmerich, M.T., Giannakoglou, K.C., Naujoks, B., 2006. Single-and multiobjective evolutionary optimization assisted by gaussian random field metamodels. IEEE Transactions on Evolutionary Computation 10, 421–439.

Fasse, G., Becker, F., Hauville, F., Astolfi, J.A., Germain, G., 2022. An experimental blade-controlled platform for the design of smart cross-flow propeller. Ocean Engineering 250, 110921.

Fonseca, C.M., Fleming, P.J., 1998. Multiobjective optimization and multiple constraint handling with evolutionary algorithms. i. a unified formulation. IEEE Transactions on Systems, Man, and Cybernetics-Part A: Systems and Humans 28, 26–37.

Gaurier, B., Davies, P., Deuff, A., Germain, G., 2013. Flume tank characterization of marine current turbine blade behaviour under current and wave loading. Renewable Energy 59, 1–12.

Huang, R., Luo, X., Ji, B., Wang, P., Yu, A., Zhai, Z., Zhou, J., 2015. Multi-objective optimization of a mixed-flow pump impeller using modified nsga-ii algorithm. Science China technological sciences 58, 2122–2130.

Jones, D.R., Schonlau, M., Welch, W.J., 1998. Efficient Global Optimization of Expensive Black-Box Functions. Journal of Global optimization 13, 455–492.

Keane, A.J., 2006. Statistical improvement criteria for use in multiobjective design optimization. AIAA journal 44, 879–891.

Kleijnen, J.P., 2009. Kriging metamodeling in simulation: A review. European Journal of Operational Research 192, 707 – 716.

Lim, H., Kim, H., 2019. Multi-objective airfoil shape optimization using an adaptive hybrid evolutionary algorithm. Aerospace Science and Technology 87, 141–153.

Luo, C., Shimoyama, K., Obayashi, S., 2014. Kriging model based many-objective optimization with efficient calculation of expected hypervolume improvement, in: 2014 IEEE Congress on Evolutionary Computation (CEC), IEEE. pp. 1187–1194.

Meliani, M., Bartoli, N., Lefebvre, T., Bouhlel, M.A., Martins, J., Morlier, J., 2019. Multi-fidelity efficient global optimization : Methodology and application to airfoil shape design, in: AIAA Aviation 2019 Forum,Dallas, United States.

Passos, A.G.d., Luersen, M.A., 2018. Multiobjective optimization of laminated composite parts with curvilinear fibers using kriging-based approaches. Structural and Multidisciplinary Optimization 57, 1115–1127.

Picheny, V., 2015. Multiobjective optimization using gaussian process emulators via stepwise uncertainty reduction. Statistics and Computing 25, 1265–1280.

Picheny, V., Wagner, T., Ginsbourger, D., 2013. A benchmark of kriging-based infill criteria for noisy optimization. Structural and Multidisciplinary Optimization 48, 607–626.

Rasmussen, C.E., Williams, C.K.I., 2006. Gaussian Processes for Machine Learning. MIT Press.

Roesler, B.T., Kawamura, M.L., Miller, E., Wilson, M., Brink-Roby, J., Clemmenson, E., Keller, M., Epps, B.P., 2016. Experimental performance of a novel trochoidal propeller. Journal of Ship Research 60, 48–60.

Sacher, M., Durand, M., Berrini, E., Hauville, F., Duvigneau, R., Le Maître, O., Astolfi, J.A., 2018a. Flexible hydrofoil optimization for the 35th america's cup with constrained ego method. Ocean Engineering 157, 62–72.

Sacher, M., Duvigneau, R., Le Maitre, O., Durand, M., Berrini, E., Hauville, F., Astolfi, J.A., 2018b. A classification approach to efficient global optimization in presence of non-computable domains. Structural and Multidisciplinary Optimization 58, 1537–1557.

Sacher, M., Hauville, F., Duvigneau, R., Le Maître, O., Aubin, N., Durand, M., 2017a. Efficient optimization procedure in non-linear fluid-structure interaction problem: Application to mainsail trimming in upwind conditions. Journal of Fluids and Structures 69, 209–231.

Sacher, M., Hauville, F., Duvigneau, R., Le Maître, O., Aubin, N., Durand, M., 2017b. Efficient optimization procedure in non-linear fluid-structure interaction problem: Application to mainsail trimming in upwind conditions. Journal of Fluids and Structures 69, 209 – 231.

Schneider, E., 1928. Blade wheel. US Patent 1681500. URL: https://patents.google.com/patent/US1681500.

Simpson, T., Poplinski, J., Koch, N.P., Allen, J., 2001. Metamodels for computer-based engineering design: Survey and recommendations. Engineering with Computers 17, 129–150.

Svenson, J.D., Santner, T.J., 2010. Multiobjective optimization of expensive black-box functions via expected maximin improvement. The Ohio State University, Columbus, Ohio 32.

Theotokatos, G., Tzelepis, V., 2015. A computational study on the performance and emission parameters mapping of a ship propulsion system. Proceedings of the Institution of Mechanical Engineers, Part M: Journal of Engineering for the Maritime Environment 229, 58–76.

Triantafyllou, M.S., Techet, A.H., Hover, F.S., 2004. Review of experimental work in biomimetic foils. IEEE Journal of Oceanic Engineering 29, 585–594.

Wagner, T., Emmerich, M., Deutz, A., Ponweiser, W., 2010. On expected-improvement criteria for model-based multi-objective optimization, in: International Conference on Parallel Problem Solving from Nature, Springer. pp. 718–727.

Zhan, D., Cheng, Y., Liu, J., 2017. Expected improvement matrix-based infill criteria for expensive multiobjective optimization. IEEE Transactions on Evolutionary Computation 21, 956–975.